*electronics*

MDPI

*Article*

# An Efficiency Improvement Strategy for Triple-Active-Bridge-Based DC Energy Routers in DC Microgrids

**Xiaoli Meng [1], Qing Duan [1], Guanglin Sha [1], Caihong Zhao [1], Haoqing Wang [1], Xueli Wang [2] and Zheng Lan [2,*]**

[1] China Electric Power Research Institute, Beijing 100192, China; mengxl@epri.sgcc.com.cn (X.M.); duanqing@epri.sgcc.com.cn (Q.D.); shaguanglin@epri.sgcc.com.cn (G.S.); zhaocaihong@epri.sgcc.com.cn (C.Z.); wanghaoqing@epri.sgcc.com.cn (H.W.)

[2] College of Electrical and Information Engineering, Hunan University of Technology, Zhuzhou 412007, China; wangxueli@stu.hut.edu.cn

* Correspondence: lan@hut.edu.cn; Tel.: +86-189-7514-2328

**Abstract:** A triple-active bridge (TAB) can be used as a power conversion unit in a three-port DC energy router (DCER) such as a triple-active bridge-based DC energy router (TAB-DCER). The operational loss of a TAB can be seen as a key factor affecting the efficiency of a TAB-DCER. However, the RMS value of the inductor current of the TAB-DCER increases under single-phase shift (SPS) control, and this greatly increases the system operating losses. The use of phase-shifted plus PWM (PS-PWM) control can reduce the RMS value of the inductor current, but its mathematical model is complex, and involves difficult calculations. To address this problem, in the study reported here, we developed an optimal control strategy for the RMS value of the inductor current based on TAB-DCER. First, the working principle of a TAB-DCER under PS-PWM control was analyzed, and a circuit decomposition model was established. Second, the operating modes under PS-PWM control were analyzed, and corresponding expressions of port power and the RMS value of the inductor current were obtained. Third, an optimized mathematical model of the sum of squares of the RMS value of the inductor current of the TAB-DCER was constructed. Finally, a genetic algorithm was used to solve the mathematical model and derive the optimal phase shift angle; this resulted in a lower RMS value of the inductor current in the TAB-DCER and reduced the system operating losses. The simulation and experimental results show that the TAB-DCER used in the present study can reduce operating losses, improve system efficiency, and deliver coordinated power control.

**Keywords:** DC energy router; triple-active bridge; inductor current optimization; genetic algorithm; phase-shifted plus PWM



**Citation:** Meng, X.; Duan, Q.; Sha, G.; Zhao, C.; Wang, H.; Wang, X.; Lan, Z. An Efficiency Improvement Strategy for Triple-Active-Bridge-Based DC Energy Routers in DC Microgrids. *Electronics* **2024**, *13*, 1172. https://doi.org/10.3390/electronics13071172

Academic Editor: Raffaele Giordano

Received: 8 February 2024
Revised: 5 March 2024
Accepted: 7 March 2024
Published: 22 March 2024



## 1. Introduction

With recent large-scale growth in distributed renewable energy sources, electric vehicles, and energy storage systems connected to power systems, DC microgrids may represent the best possible access solution. Adjacent DC microgrids can be interconnected to form a DC microgrid group which is characterized by complementarity and coordination among distributed energy sources; this, in turn, can improve the reliability of the power supply. Levels of performance with respect to interconnection, energy scheduling, and coordinated methods can be seen as key factors in determining whether mutual support control can be achieved between different DC microgrids [1,2]. A triple-active bridge-based DC energy router (TAB-DCER) can interconnect three adjacent DC microgrids and achieve a reasonable distribution of energy among multiple DC microgrids. A TAB-DCER can also be used to realize a flexible coordination of renewable energy and storage across regions and further realize complementary energy support [3–5]. Figure 1 presents a schematic diagram of the structure of an interconnected multiple DC microgrid system based on a TAB-DCER.

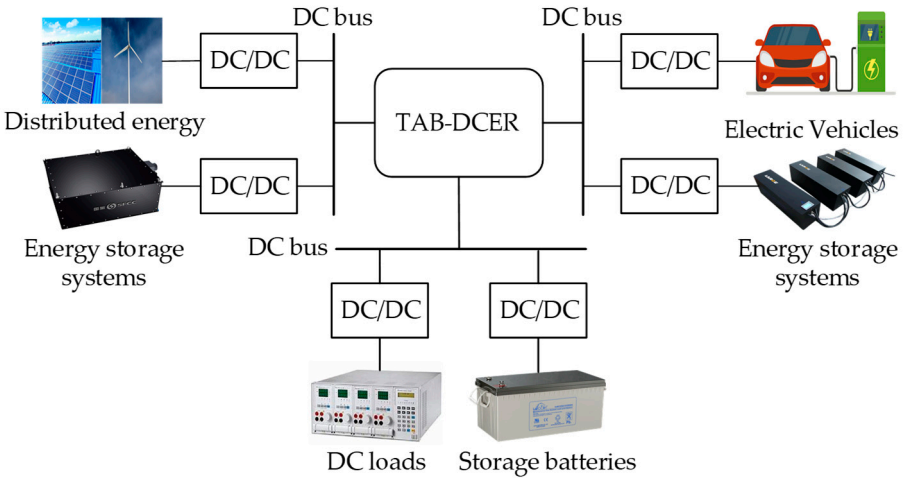


**Figure 1.** Multi-DC microgrid interconnection system based on TAB-DCER.

Single-phase shift control (SPS) is the most basic control strategy of a TAB-DCER. Using an SPS control strategy, the authors of [6,7] analyzed expressions of port power in different operating modes and used model predictive control to achieve port power decoupling. The authors of [8,9] eliminated the AC component of the current and carried out a real-time calculation of the decoupling phase shift angle to reduce the power coupling between ports. The authors of [10] proposed an active damping method that not only achieved port power decoupling but also effectively eliminated oscillation in the TAB-DCER's input current. The authors of [11] designed a structure for a multi-resonant TAB-DCER; this realized power decoupling and also improved the efficiency of the system. However, this method is suitable only for TAB-DCER converters with specific resonant structures. In some related studies [6–11], the efficiency of the TAB-DCER was not assessed. The authors of [12,13] analyzed the ZVS condition of a TAB-DCER in detail, but these analyses were only based on SPS control, which is characterized by limited control degrees of freedom and low flexibility. In addition, and as reported in the literature [14], in the presence of return power, the RMS value of the inductor current increases, increasing the loss in the TAB-DCER and reducing the operational efficiency of the system. The authors of [15] proposed a phase-shifted plus PWM (PS-PWM) control strategy; this was found to effectively reduce the system operating losses and improve operational efficiency. The authors of [16] briefly analyzed the ZVS of all switching modes under PS-PWM control; such control was found to broaden the ZVS range and improve the system's efficiency. However, these authors did not analyze the efficiency of the TAB-DCER from the perspective of the RMS value of the inductor current. In addition, due to the increase in control degrees of freedom obtained under the PS-PWM control strategy, the mathematical model of the TAB-DCER becomes more complex, making it difficult to analyze and solve using the traditional modal analysis method. The authors of [17] proposed a simple unified solution model for a TAB-DCER inductor current. By such means, a unified expression for an inductor current was derived, and the difficulty of analysis was reduced. In another study [18], a frequency domain-generalized harmonic approximation technique was used to optimize the RMS value of the inductor current. However, such a technique cannot be used to determine the expression of the inductor current in the time domain.

To make the RMS current easier to calculate in the time domain, the intelligent optimization algorithm may be of potential utility [19–24]. In some recent studies [19–21], researchers used particle swarm optimization and a genetic algorithm to calculate the phase shift angle of DAB to optimize the RMS value of the inductor current and the current stress. In another study [22], a multi-objective and comprehensive control strategy to optimize efficiency was proposed; this can not only achieve soft switching of a TAB-DCER, but also reduce current RMS and loss. The authors of [23] used a neural network to optimize the RMS value of the inductor current and thus reduce system losses. Finally, the authors of [24]

compared the effectiveness of methods such as an offline gradient descent search and an artificial neural network for optimization of the RMS value of the inductor current. Using an intelligent optimization algorithm, the appropriate phase shift angle for all operating conditions of the DC–DC converter can be calculated and embedded in the program code for the controller to look up the table; this effectively reduces the number of real-time calculations. Compared with a control algorithm of the real-time computing class, the design of the system was simplified, and calculation speed was increased. No applications of a genetic algorithm for TAB modulation were found in the literature.

In summary, in the present study, we focused on creating an efficiency improvement strategy for a three-port energy router in DC microgrids. A circuit decomposition model of a TAB-DCER under PS-PWM control was constructed, and a unified expression of the power and the RMS value of the inductor current of each port under different working modes was obtained. An optimal mathematical model of the sum of squares of the RMS value of the inductor current for each port was constructed to calculate the appropriate phase shift angle to reduce the system operating losses using the genetic algorithm. Using the proposed strategy, it was found that a TAB-DCER can quickly adjust load power, maintain stable operation of the system, achieve power coordinated control, optimize the levels of the system operating losses, and achieve high-efficiency operation. The feasibility and effectiveness of the proposed strategy were then verified by experiments.

## 2. The Topology and Working Principle of TAB-DCER

The TAB-DCER topology is shown in Figure 2. Each port is connected to a high-frequency transformer via three H-bridge modules. The presence of the high-frequency transformer provides electrical isolation to the ports. When a short-circuit fault occurs at one port, the short-circuit inrush current does not flow through the DC bus to the other ports. This system also enables port interconnections at various voltage levels by adjusting the transformer turns ratio. The TAB-DCER converter is safe and stable and delivers high-efficiency energy conversion.

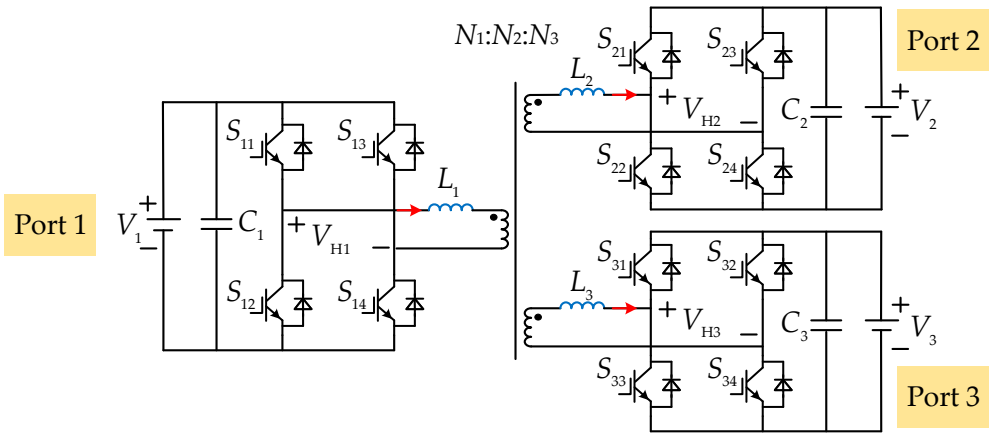


**Figure 2.** Topological diagram of the TAB-DCER.

In the present study, we define the output power flow of port one and the input power flows of ports two and three as being in a positive direction. $L_1$, $L_2$, and $L_3$ represent the power transfer inductance of ports one, two, and three, respectively, and the transformer winding ratio is $N_1 : N_2 : N_3$. For ease of analysis, ports two and three are commuted to the port one side to obtain the Δ-type and Y-type equivalent circuits of the TAB-DCER, as shown in Figure 3.

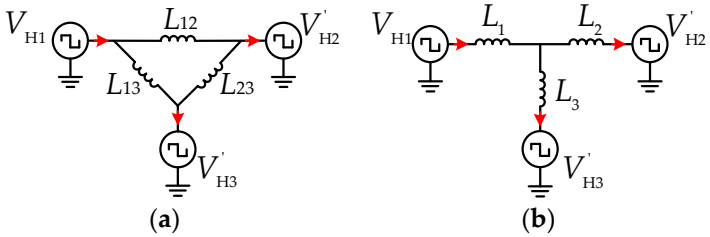


**Figure 3.** Equivalent circuits of TAB-DCER. (**a**) △-equivalent circuit. (**b**) Y-equivalent circuit.

### *2.1. Control Strategy of TAB-DCER*

#### 2.1.1. SPS Control Strategy

The SPS control strategy of TAB-DCER regulates the output power of each port by controlling the phase shift angle, $\varphi_{ij}$, between the square-wave voltages, $V_{\mathrm{H}i}(i = 1, 2, 3)$, of the H-bridge at each port. The operating waveforms of the H-bridge square-wave voltage at each port under SPS control are shown in Figure 4. The transmitted power between each port can be adjusted simply by adjusting the size of the phase shift angle.

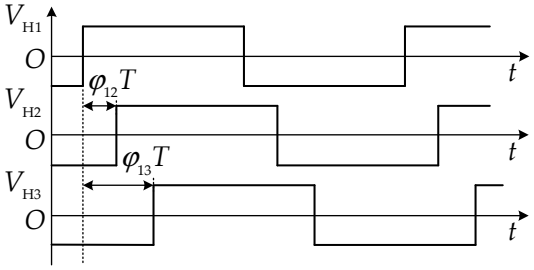


**Figure 4.** SPS control strategy for TAB-DCER converters.

The transmission power of each port is determined to have the maximum value, $P_{\mathrm{max}ij}$, when $\varphi_{ij} = 0.5$ under SPS control, as shown in Equation (1).

$$P_{\mathrm{max}ij} = \frac{n_{ij} V_i V_j}{8 f_{\mathrm{s}} L_{ij}} \tag{1}$$

Here, $n_{ij} = N_i / N_j$, $f_{\mathrm{s}}$ is the switching frequency, and $L_{ij}$ is the inductance in the Δ-type equivalent circuit.

#### 2.1.2. Phase-Shifted Plus PWM Control

PS-PWM control of TAB-DCER introduces an inward phase shift angle, $\delta_i(i = 1, 2, 3)$, based on the SPS control, as shown in Figure 5. This is because control of the duty cycle of $V_{\mathrm{H}i}$ is added under the SPS control strategy. Under the phase shift plus pulse width control strategy, there are various values and combinations of the internal shift ratio $\delta_i(i = 1, 2, 3)$ at each port of the TAB-DCER. In addition, there is increased freedom of TAB-DCER control, making it more flexible. The range of values of $\delta_i(i = 1, 2, 3)$ satisfies $0 \leq \delta_i \leq 1$.

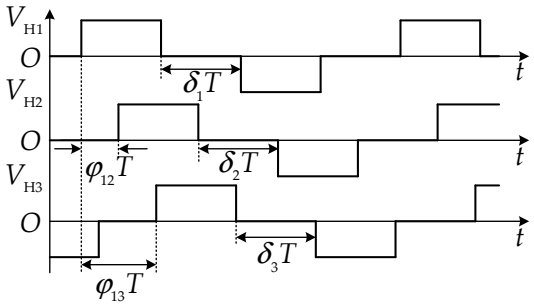


**Figure 5.** PS-PWM control strategy for TAB-DCER converters.

### *2.2. Power Flow Analysis of TAB-DCER-based DC Microgrids*

DC microgrids contain distributed energy sources such as photovoltaics and wind turbines. The output of these distributed energy sources may be affected by weather and other factors. They may also exhibit seasonal and spatial fluctuations in electrical loads. TAB-DCER enables bi-directional power flow between ports. The power-flow schematic of the TAB-DCER-based DC microgrid is shown in Figure 6.

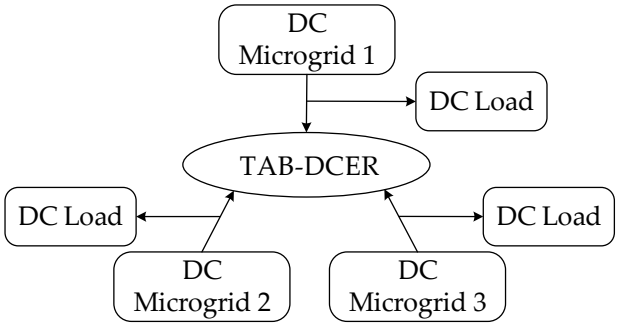


**Figure 6.** Schematic diagram of power flow in TAB-DCER-based DC microgrids.

To maximize the use of distributed energy resources and achieve a rational power distribution among the DC microgrids. TAB-DCER can quickly regulate the power of each DC grid and load according to the load connected to each port, thus maintaining the internal power balance of the system when the load changes and delivering coordinated control of the system's power.

## 3. Optimal Control of the RMS Value of the Inductor Current for TAB-DCER

The TAB-DCER can effectively convert and distribute energy between different ports, realize the coordinated control of the power of the system, and ensure the efficient use of energy. Therefore, in order to improve the efficiency of the three-port DC energy router, we propose in this paper an optimal control strategy for the RMS value of the inductor current based on the TAB-DCER. Use of this strategy can effectively reduce the RMS value of the inductor current, reduce losses, and improve system efficiency.

### *3.1. The Optimal Mathematical Model of the RMS Value of the Inductor Current for TAB-DCER Based on Circuit Decomposition*

According to Figure 5, the $V_{Hi}$ are all three-electrode square waves with a duty cycle of $1-\delta_i$ under the control of PS-PWM. As shown in Figure 7, a three-electrode square wave can be decomposed into two symmetrical two-electrode square waves. $S(t)$ is a two-electrode square-wave function with amplitude 0.5 and period $2T$, and $S(t-dT)$ is a two-electrode square-wave function with phase lag $S(t)$. Therefore, a three-electrode square wave with a duty cycle of $1-\delta_i$ can be expressed as the sum of $S(t)$ and $S(t-dT)$ with an amplitude of 1 and a period of $2T$.

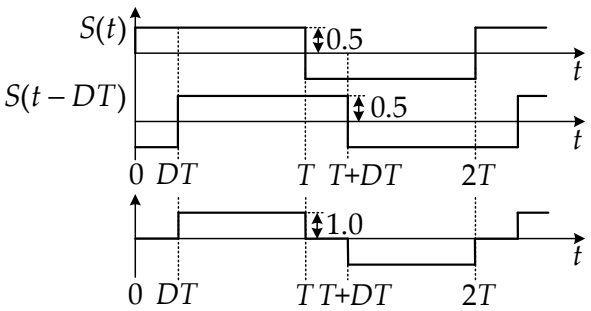


**Figure 7.** Synthesis of a two-electrode square wave into a three-electrode square wave.

$V_{\mathrm{H}i}$ under the control of PS-PWM can be expressed as shown in Equation (2).

$$\begin{cases} V_{\mathrm{H1}} = V_1\left[S(t) + S\left(t - \frac{\delta_1}{\pi}T\right)\right] \\ V_{\mathrm{H2}} = V_2\left[S\left(t - \frac{\varphi_{12}-\delta_2}{\pi}T\right) + S\left(t - \frac{\varphi_{12}}{\pi}T\right)\right] \\ V_{\mathrm{H3}} = V_3\left[S\left(t - \frac{\varphi_{13}-\delta_3}{\pi}T\right) + S\left(t - \frac{\varphi_{13}}{\pi}T\right)\right] \end{cases} \tag{2}$$

Here, $S(t)$ denotes the standard two-level square-wave function, $V_1$ is the amplitude of the input DC voltage $V_{\mathrm{H1}}$, $V_2$ is the amplitude of the DC voltage $V_{\mathrm{H2}}$ of port two, and $V_3$ is the amplitude of the DC voltage $V_{\mathrm{H3}}$ of port three.

The equivalent circuit after the decomposition of the TAB-DCER circuit can be transformed under the control of PS-PWM, as shown in Figure 8.

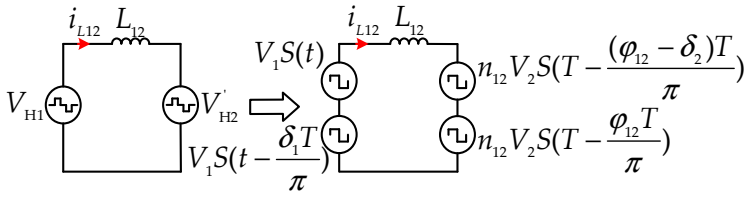


**Figure 8.** Equivalent model of the decomposed TAB-DCER circuit (taking ports one and two as examples).

To simplify the analysis, we assume that the switching devices and the magnetic components in the circuit are both ideal. According to Figure 8, the differential equation for the inductor current after the circuit decomposition can be expressed as:

$$\begin{cases} L_{12}\frac{\mathrm{d}i_{\mathrm{L12}}}{\mathrm{d}t} = V_{\mathrm{H1}} - n_{12}V_{\mathrm{H2}} \\ L_{13}\frac{\mathrm{d}i_{\mathrm{L13}}}{\mathrm{d}t} = V_{\mathrm{H1}} - n_{13}V_{\mathrm{H3}} \\ L_{23}\frac{\mathrm{d}i_{\mathrm{L23}}}{\mathrm{d}t} = n_{12}V_{\mathrm{H2}} - n_{13}V_{\mathrm{H3}} \end{cases} \tag{3}$$

Substituting Equation (2) into Equation (3), the expression for each port's inductor current can be solved based on the volt-second balance of the inductor, i.e., Equation (4):

$$\begin{cases} i_{\mathrm{L12}}(t) = \frac{V_1}{L_{12}}S_1(t) - \frac{n_{12}V_2}{L_{12}}S_2(t) \\ i_{\mathrm{L13}}(t) = \frac{V_1}{L_{13}}S_1(t) - \frac{n_{13}V_3}{L_{13}}S_3(t) \\ i_{\mathrm{L23}}(t) = \frac{n_{12}V_2}{L_{23}}S_2(t) - \frac{n_{13}V_3}{L_{23}}S_3(t) \end{cases} \tag{4}$$

where

$$\begin{cases} S_1(t) = Tr(t) - Tr(t - \delta_1 T/\pi) \\ S_2(t) = Tr(t - (\varphi_{12} - \delta_2)T/\pi) - Tr(t - \varphi_{12}T/\pi) \\ S_3(t) = Tr(t - (\varphi_{13} - \delta_3)T/\pi) - Tr(t - \varphi_{13}T/\pi) \end{cases} \tag{5}$$

Because the inductor current waveform exhibits half-period central symmetry, $Tr(t)$ is a symmetric triangular wave with amplitude $0.25T$ and period $2T$ obtained by integrating $S(t)$.

The addition of three internal phase shifts increases the number of variables and makes the analysis more complicated. For analytical purposes, in this paper, we only consider the case of adding a single internal phase shift $\delta_2$ (i.e., $\delta_1 = \delta_3 = 0, \delta_2 \neq 0$). According to the relationship between the control quantities, $\varphi_{12}, \varphi_{13}, \delta_2$, the PS-PWM control mode

can be divided into five operating modes, as shown in Figure 9. The transmission power expression of each port can be expressed as:

$$P_{ij} = \frac{1}{T}\int_0^T V_{\mathrm{H}i} i_{\mathrm{L}ij} dt \tag{6}$$

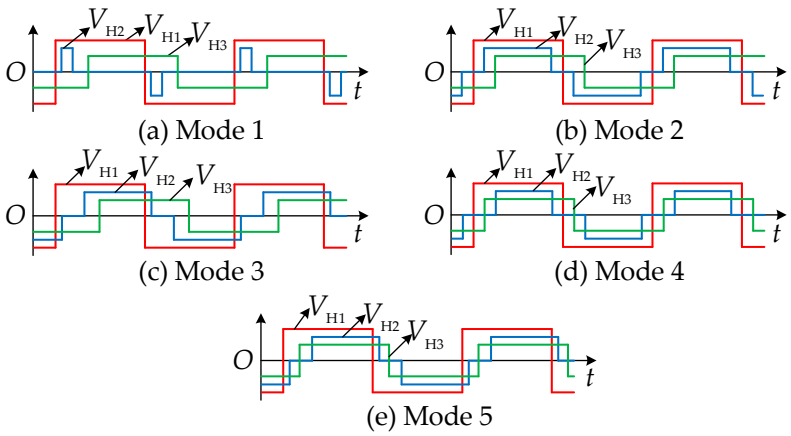


**Figure 9.** Five operating modes under PS-PWM control.

According to the power transfer relationships between each port, the power expression of each port in each of the five operating modes can now be expressed as follows:

- Mode 1, $0 < \varphi_{12} < \varphi_{13} < 1, 0 < \varphi_{12} + 1 - \delta_2 < \varphi_{13}$

$$\begin{cases} P_1 = \frac{TV_1^2}{2L_\Delta}[(1-\delta_2)(2\varphi_{12}-\delta_2) + 2\varphi_{13}(1-\varphi_{13})] \\ P_2 = \frac{TV_1^2}{2L_\Delta}(1-\delta_2)(4\varphi_{12}-2\varphi_{13}-2\delta_2) \\ P_3 = \frac{TV_1^2}{2L_\Delta}[2\varphi_{13}(1-\varphi_{13}) - (1-\delta_2)(2\varphi_{12}-2\varphi_{13}-\delta_2)] \end{cases} \tag{7}$$

- Mode 2, $0 < \varphi_{12} < \varphi_{13} < 1, \varphi_{13} < \varphi_{12} + 1 - \delta_2 < 1$

$$\begin{cases} P_1 = \frac{TV_1^2}{2L_\Delta}[(1-\delta_2)(2\varphi_{12}-\delta_2) + 2\varphi_{13}(1-\varphi_{13})] \\ P_2 = \frac{TV_1^2}{2L_\Delta}(2\varphi_{13} - 2\varphi_{13}\delta_2 - 2\varphi_{12}^2 - 2\varphi_{13}^2 + 4\varphi_{12}\varphi_{13}) \\ P_3 = \frac{TV_1^2}{2L_\Delta}(2\varphi_{12} - \delta_2 - 2\varphi_{12}\delta_2 + 2\varphi_{13}\delta_2 + \delta_2^2 + 2\varphi_{12}^2 - 4\varphi_{12}\varphi_{13}) \end{cases} \tag{8}$$

- Mode 3, $0 < \varphi_{12} < \varphi_{13} < 1, \varphi_{12} - \delta_2 > 0$

$$\begin{cases} P_1 = \frac{TV_1^2}{2L_\Delta}[-(2\varphi_{12}^2 + \delta_2^2 - 2\varphi_{12} + \delta_2 - 2\varphi_{12}\delta_2) + 2\varphi_{13}(1-\varphi_{13})] \\ P_2 = \frac{TV_1^2}{2L_\Delta} = [2\varphi_{13} + 4\varphi_{12}\delta_2 - 2\varphi_{13}\delta_2 - 2\delta_2^2 - 4\varphi_{12}^2 - 2\varphi_{13}^2 + 4\varphi_{12}\varphi_{13}] \\ P_3 = \frac{TV_1^2}{2L_\Delta}(2\varphi_{12} - \delta_2 - 2\varphi_{12}\delta_2 + 2\varphi_{13}\delta_2 + \delta_2^2 + 2\varphi_{12}^2 - 4\varphi_{12}\varphi_{13}) \end{cases} \tag{9}$$

- Mode 4, $0 < \varphi_{13} < \varphi_{12} < 1, \varphi_{13} < \varphi_{12} + 1 - \delta_2 < 1$

$$\begin{cases} P_1 = \frac{TV_1^2}{2L_\Delta}[(1-\delta_2)(\delta_2 - 2\varphi_{12}) + 2\varphi_{13}(1-\varphi_{13})] \\ P_2 = \frac{TV_1^2}{2L_\Delta}(1-\delta_2)(-2\varphi_{12} - 2\varphi_{13}) \\ P_3 = \frac{TV_1^2}{2L_\Delta}[2\varphi_{13}(1-\varphi_{13}) + (1-\delta_2)(2\varphi_{13} + \delta_2)] \end{cases} \tag{10}$$

- Mode 5, $0 < \varphi_{13} < \varphi_{12} < 1$, $\varphi_{12} - \delta_2 > 0$

$$\begin{cases} P_1 = \frac{TV_1^2}{2L_\Delta}\left[-\left(2\varphi_{12}^2 + \delta_2^2 - 2\varphi_{12} + \delta_2 - 2\varphi_{12}\delta_2\right) + 2\varphi_{13}(1-\varphi_{13})\right] \\ P_2 = \frac{TV_1^2}{2L_\Delta}\left[\left(-2\varphi_{12}^2 + 4\varphi_{12} - 2\delta_2\right) - 2\varphi_{13} + 2\varphi_{13}\delta_2\right] \\ P_3 = \frac{TV_1^2}{2L_\Delta}\left[2\varphi_{13}(1-\varphi_{13}) - (1-\delta_2)(2\varphi_{12} - 2\varphi_{13} - \delta_2)\right] \end{cases} \tag{11}$$

According to the calculation formula for the RMS current:

$$I^2 = \frac{1}{T}\int_0^T i^2(t)\,\mathrm{d}t \tag{12}$$

the expression of the RMS value of the inductor current based on the circuit decomposition model can be calculated:

$$\begin{cases} I_{L12}^2 = \frac{T^2V_1^2}{\pi^2L^2}\left(\varphi_{12}^2 + \frac{1}{4}\delta_2^2 - \varphi_{12}\delta_2\right) \\ I_{L23}^2 = \frac{T^2V_1^2}{\pi^2L^2}\left(\varphi_{12}^2 + \varphi_{13}^2 + \frac{1}{4}\delta_2^2 - \varphi_{12}\delta_2 - 2\varphi_{12}\varphi_{13} + \varphi_{13}\delta_2\right) \\ I_{L13}^2 = \frac{T^2V_1^2}{\pi^2L^2}\varphi_{13}^2 \end{cases} \tag{13}$$

where $L = L_{12} = L_{13} = L_{23}$.

According to the expression

$$I_{\mathrm{RMS}}^2 = I_{L12}^2 + I_{L23}^2 + I_{L13}^2 \tag{14}$$

we can now obtain an expression for the sum of squares of the RMS value of the inductor current based on the circuit decomposition model as follows:

$$I_{\mathrm{RMS}}^2 = \frac{T^2V_1^2}{\pi^2L^2}\left(2\varphi_{12}^2 + 2\varphi_{13}^2 + \frac{1}{2}\delta_2^2 - 2\varphi_{12}\delta_2 - 2\varphi_{12}\varphi_{13} + \varphi_{13}\delta_2\right) \tag{15}$$

The optimal mathematical model of the sum of squares inductor RMS current based on the circuit decomposition algorithm can now be expressed as follows:

$$\begin{cases} \min \quad I_{\mathrm{RMS}}^2 = f(\varphi_{12}, \varphi_{13}, \delta_2) \\ s.t. g\left(\varphi_{12}, \varphi_{13}, \delta_2, P_i^*\right) = 0 \\ \qquad l_j(\varphi_{12}, \varphi_{13}, \delta_2) \le 0 \end{cases} \tag{16}$$

where $f(\varphi_{12}, \varphi_{13}, \delta_2)$ is the expression of the sum of squares of the RMS value of the inductor current, $g(\varphi_{12}, \varphi_{13}, \delta_2) = 0$ is the port power constraint, and $l_j$ is the phase shift angle constraint in the operating mode $j$.

For analytical purposes, the power reference value and the reference value of the sum of squares of the RMS value of the inductor current are as follows:

$$P_{\mathrm{b}} = \frac{TV_1^2}{2\pi L},\ I_{\mathrm{b}}^2 = \frac{T^2V_1^2}{4\pi^2L^2} \tag{17}$$

### *3.2. Optimal Control of the RMS Value of the Inductor Current*

Because multiple combinations of phase shift angles may give the same power output under PS-PWM control, algorithms must be combined to determine the optimal combination that minimizes the RMS value of the inductor current. The genetic algorithm is an optimization algorithm that simulates natural selection. Local optimization results can be effectively avoided by adjusting the initial parameters of the genetic algorithm.

The specific process of the genetic algorithm is shown in Figure 10, including coding, decoding, genetic operation, fitness calculation, evaluation, etc. The initialization parameters are shown in Table 1. First, the parameters of the genetic algorithm are initialized. The initial parameters $(\varphi_{12}, \varphi_{13}, \delta_2)$ are obtained for each individual in the population, and fitness is calculated. The individuals are then encoded. Next, selection, crossover, and mutation operations are performed on the population according to the set parameters; the new population after the operations is then decoded. The fitness of this iteration is compared with the optimal fitness, and the better result is used to update the optimal fitness and optimal solution. Finally, the operation is ended when the termination principle is satisfied.

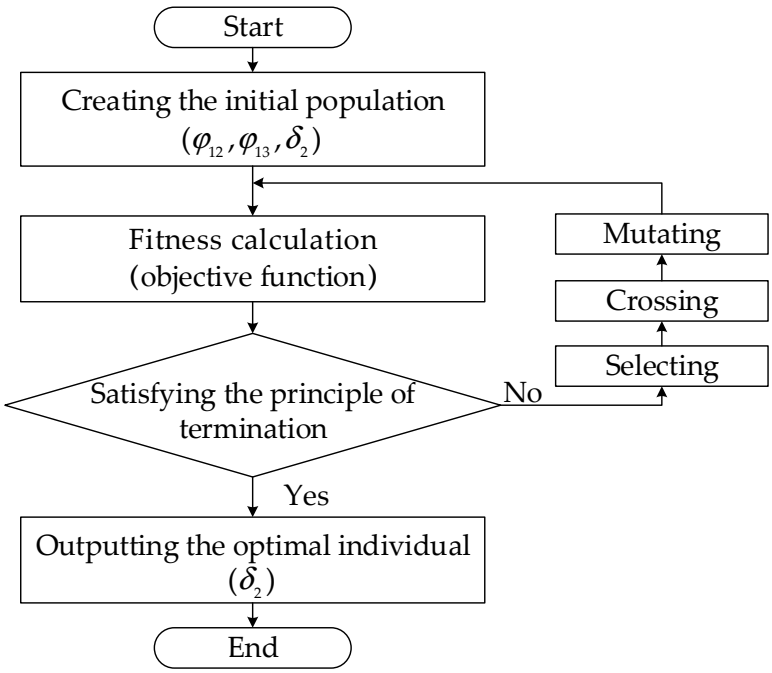


**Figure 10.** Genetic algorithm flowchart.

**Table 1.** Initial parameters of the genetic algorithm.

| Parameter | Numeric Value |
|---|---|
| Population size | 100 |
| Evolutionary algebra | 50 |
| Crossover probability | 0.6 |
| Probability of variation | 0.01 |

Figure 10 shows a flowchart of the genetic algorithm optimization strategy (GAOS) for an inductor current based on the circuit decomposition model. Figure 11 shows a block diagram for the implementation of the GAOS for an inductor current based on the circuit decomposition model. Firstly, before the system runs, the calculation results of the genetic algorithm need to be stored in the microcontroller. We obtain the shift ratio $(\varphi_{12}, \varphi_{13})$ after passing through the PI controller by detecting the difference between the inductor current of port two and the reference value and the difference between the voltage of port three and the reference value. Next, the optimized shift ratio combination is obtained by checking the online table of $\delta_2$ based on the port power. The optimized shift ratio is input to the PWM modulation module to achieve control of the TAB-DCER.

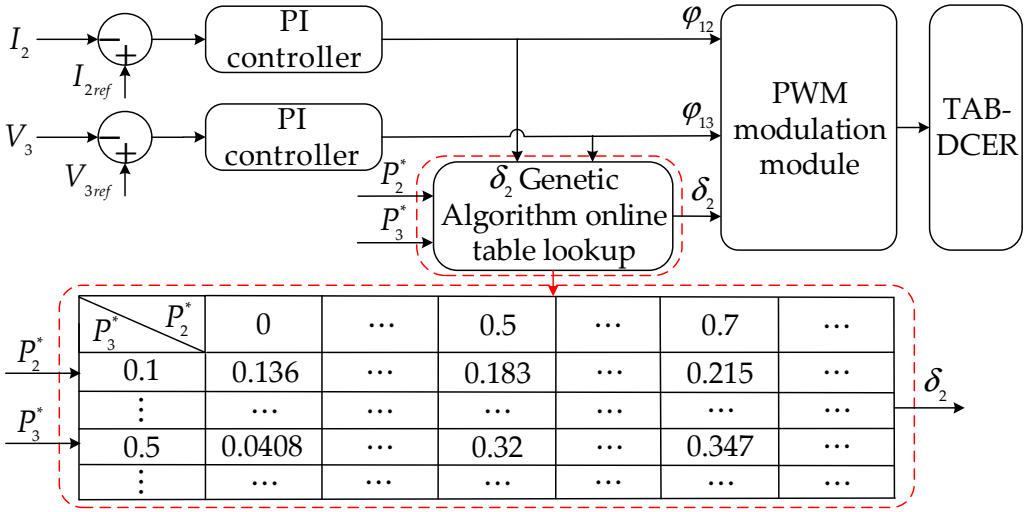


**Figure 11.** Optimal control strategy of the RMS value of the inductor current.

## 4. Simulation and Experimental Verification

### *4.1. Simulation Analysis of Power Coordination Control in TAB-DCER*

In this section, we describe the TAB-DCER simulation model based on the MATLAB/Simulink 2018b platform that we used to verify the power coordination control capability of the TAB-DCER. The main simulation parameters are shown in Table 2. Port one is connected to the DC microgrid to access the distributed micro source. Port two is connected to the DC microgrid to access the distributed micro source and load. Port three is connected to the DC microgrid to access the load. The DC bus of a DC microgrid is simulated with a DC power supply and a 0.8 Ω series resistor.

**Table 2.** Main simulation parameters.

| Parameter | Stats |
|---|---|
| Port one voltage $V_1$ (V) | 120 |
| Port two voltage $V_2$ (V) | 120 |
| Port three voltage $V_3$ (V) | 240 |
| Switching frequency $f_s$ (Hz) | 20,000 |
| Transformer ratio $N_1 : N_2 : N_3$ | 1:1:2 |
| Power transmission inductance $L_1$, $L_2$, $L_3$ (Mh) | 21.33, 21.33, 85.32 |

During normal operation, the DC microgrid load resistance of access ports two and three is set to 100 Ω and 200 Ω, respectively. Figure 12 shows the waveforms of port-power and load-power consumption in each port of TAB-DCER when there is a sudden change in load power in port two. As shown in Figure 12, the load resistance of the port two DC microgrid changes from 100 Ω to 50 Ω at 0.8 s, and then to 100 Ω at 1.6 s. As can be seen from the figure, the load power within the port three DC microgrid still maintains constant power after a short fluctuation when the load of the port two DC microgrid increases or decreases. The load fluctuation in the port two microgrid does not affect the stability of the port three DC microgrid.

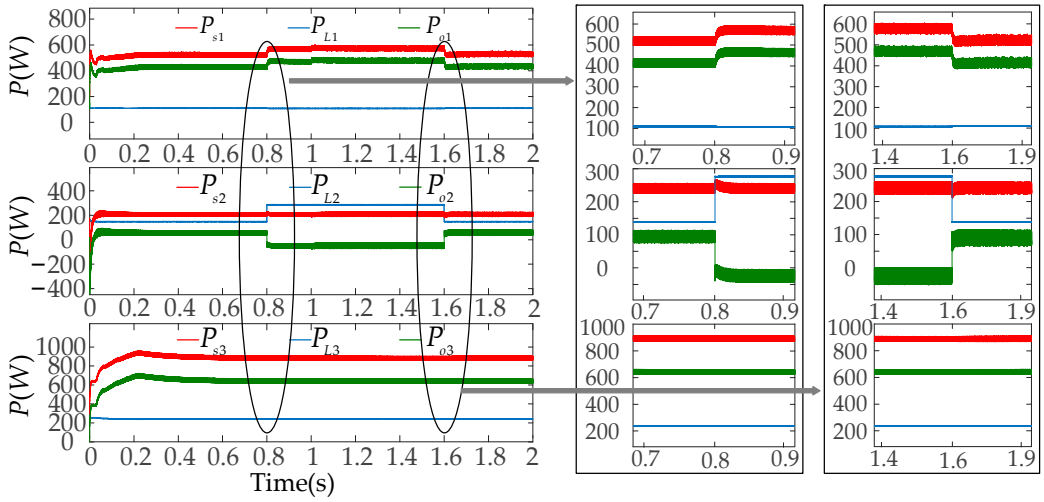


**Figure 12.** Waveforms of port-power consumption and load-power consumption in each port of TAB-DCER with a sudden load-power change in port two.

Figure 13 shows the waveforms of port-power and load-power consumption in each port of TAB-DCER when there is a sudden change in load power in port three. As can be seen in Figure 13, the load resistance of the port three DC microgrid changes from 200 Ω to 100 Ω at 0.8 s, and then to 200 Ω at 1.6 s. It can also be seen from the figure that the load power within the port two DC microgrid still maintains constant power after a short fluctuation when the load of the port three DC microgrid increases or decreases. Furthermore, this does not affect the stability of the port two DC microgrid.

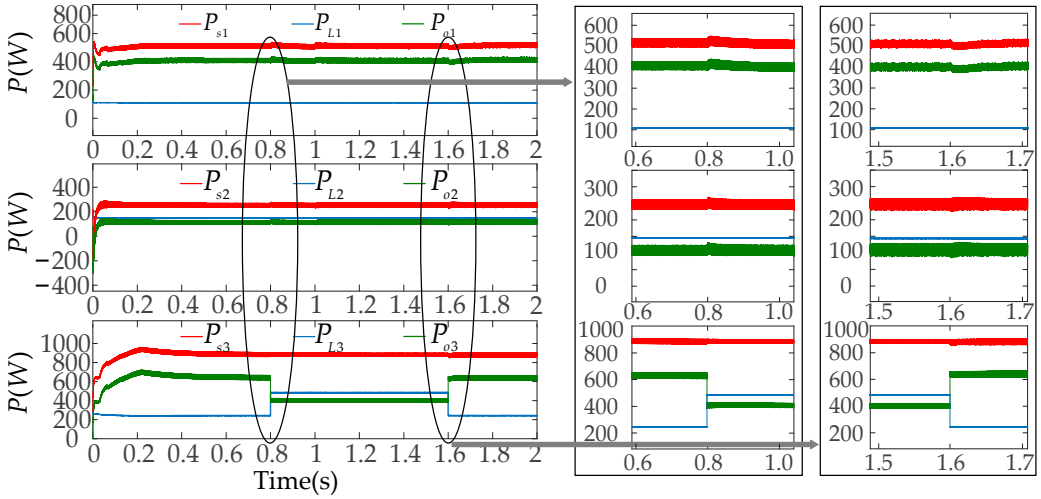


**Figure 13.** Waveforms of port-power consumption and load-power consumption in each port of TAB-DCER with a sudden load-power change in port three.

As can be seen from Figures 12 and 13, TAB-DCER is able to quickly regulate load power in the DC microgrid according to operating conditions, so that the system continues to run stably. In addition, power coordinated control is realized when the operating conditions of the system change.

### *4.2. Simulation Verification and Analysis of GAOS Control Strategy*

Figure 14 shows the three-dimensional relationship between the sum of squares of the RMS value of the inductor current ($I^2_{\mathrm{RMS}}$) and the power of ports two and three under the SPS and GAOS control strategies of TAB-DCER. It can be seen from the figure that the sum of squares of the RMS value of the inductor current is proportional to the port power

and that the $I^2_{RMS}$ is significantly smaller under the GAOS control strategy than the SPS control strategy.

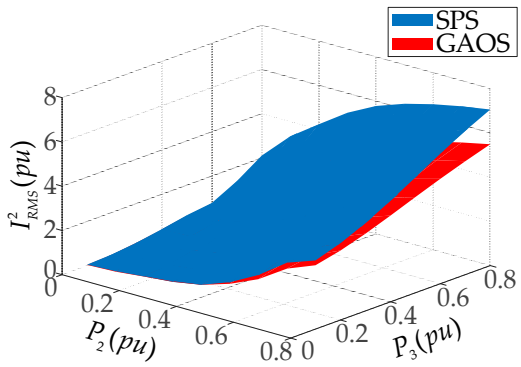


**Figure 14.** Three-dimensional plot of $I^2_{RMS}$ vs. power at each port under the two control strategies.

Figure 15 shows waveforms for voltage and inductor current at each port under both control strategies when $P_2 = 0.6$ (per unit) and $P_3 = 0.1$ (per unit). In this condition, the inward shift ratio is calculated by the GAOS control strategy as $D = 0.07$, and the sum of squares of the RMS value of the inductor current (per unit) at each port is 1.452. The sum of squares of the RMS value of the inductor current (per unit) at each port under the SPS control strategy is 1.478. In Figure 14, the optimization of the RMS value of the inductor current under GAOS control is obvious; current values are significantly smaller than those obtained under SPS control.

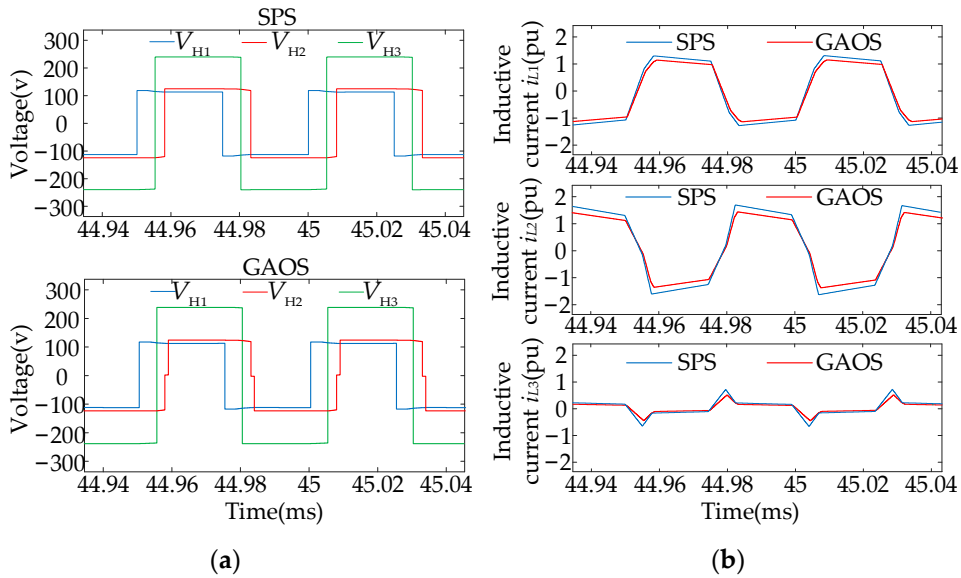


(**a**) (**b**)

**Figure 15.** Waveforms at each port with $P_2$ = 0.6 (per unit), $P_3$ = 0.1 (per unit). (**a**) Voltage waveform of each port under two control modes. (**b**) Inductor current waveform of each port under two control modes.

Figure 16 presents a schematic diagram of the input power at another port versus the sum of squares of the RMS value of the inductor current when the input power at either port two or three is constant. As shown in Figure 16a, the sum of squares of the RMS value of the inductor current is proportional to the port two input power, $P_2$, when the input power, $P_3$, at port three is constant. The sum of squares of the RMS value of the inductor current is significantly smaller under GAOS control than under SPS control. It can be seen in Figure 16b that the sum of squares of the RMS value of the inductor current is proportional to $P_3$ when the input power, $P_2$, at port two is constant. The sum of squares of the RMS value of the inductor current is significantly smaller under GAOS control than

under SPS control. As shown in Figure 16, the GAOS control strategy can effectively reduce the RMS value of the inductor current.

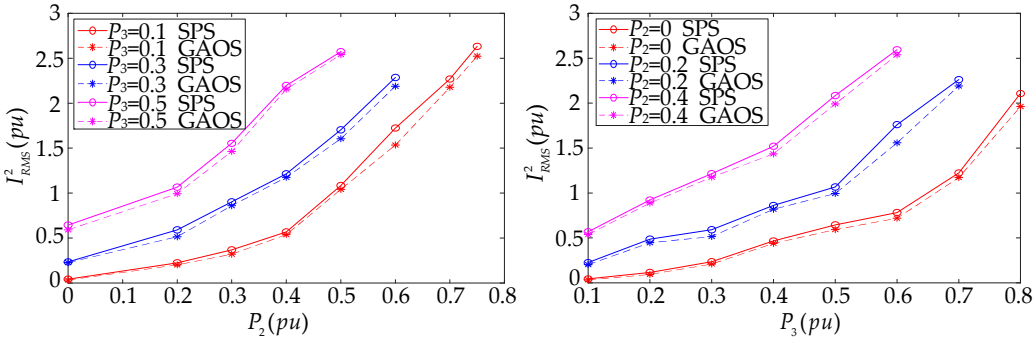


(**a**) (**b**)

**Figure 16.** Two-dimensional plot of $I^2_{\mathrm{RMS}}$ versus power at each port. (**a**) Schematic of the relationship between $P_2$ and the sum of squares of current RMS when $P_3$ is constant. (**b**) Schematic of the relationship between $P_3$ and the sum of squares of current RMS when $P_2$ is constant.

### *4.3. Experimental Validation and Analysis*

To confirm the effectiveness of the GAOS control strategy described in this paper, it was necessary to validate the experiments on a semi-physical experimental platform based on Star Sim hardware, as shown in Figure 17. The main parameters of the experiment are presented in Table 3.

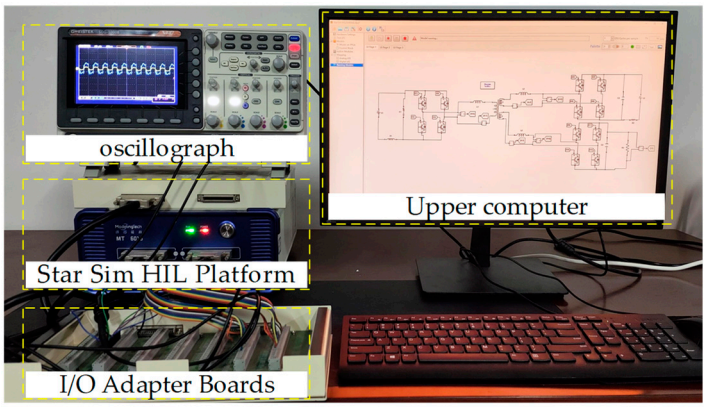


**Figure 17.** Star Sim hardware-in-the-loop semi-physical experimental platform.

**Table 3.** Main parameters of the experiment.

| Parameter | Stats |
|---|---|
| Port 1 voltage $V_1$(V) | 120 |
| Port 2 voltage $V_2$(V) | 120 |
| Port 3 voltage $V_3$(V) | 240 |
| Switching frequency $f_s$(Hz) | 5000 |
| Transformer ratio $N_1 : N_2 : N_3$ | 1:1:2 |
| Power transmission inductance $L_1$: $L_2$: $L_3$ (Mh) | 21.33 |

Figure 18 gives the experimental waveforms of each port under the two control strategies when $P_2 = 960$ W and $P_3 = 480$ W. The sum of squares of the RMS value of the inductor current (per unit) at each port for the SPS control strategy was 0.096. The sum of squares of the RMS value of the inductor current (per unit) at each port for the GAOS control strategy was 0.078. These experimental results were consistent with the simulation analysis. We conclude, therefore, that the optimized control strategy proposed in this paper

can effectively reduce the sum of squares of the RMS value of the inductor current and thus reduce conduction loss.

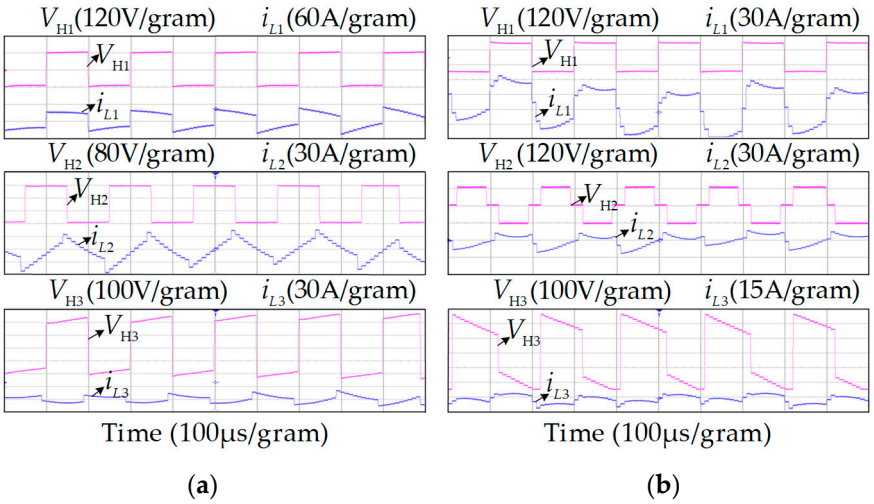


**Figure 18.** Experimental waveforms under two control strategies when $P_2$ = 960 W, $P_3$ = 480 W. (**a**) SPS control. (**b**) GAOS control.

## 5. Conclusions

Operational losses can be seen as a crucial factor affecting the efficiency of TAB-DCER converters. Under SPS control, TAB-DCER is characterized by a large RMS value of the inductor current and low operational efficiency. Under PS-PWM control, the mathematical model is complicated, and analysis of current is difficult to achieve; this also affects levels of operational loss. In the study reported in this paper, the working principle of TAB-DCER under PS-PWM control was first analyzed, and the equivalent circuit was then decomposed into a circuit in which two square-wave power supplies acted together based on the superposition theorem. Next, a unified expression for the power and the RMS value of the inductor current at each port in different operating modes was constructed. A mathematical optimization model of the sum of squares of the RMS value of the inductor current for each port was then established; this was used to calculate the appropriate phase shift angle using a genetic algorithm. It was found that TAB-DCER running at the optimal phase shift angle greatly reduced losses. Finally, an experimental platform was built to verify the feasibility and effectiveness of the control strategy. The following conclusions were drawn from the work described above:

1. The sum of squares of the RMS value of the inductor current of the TAB-DCER is related only to the phase shift angle between the ports and the duty cycle of the switching tubes. TAB-DCER can quickly adjust the load power according to the working condition to keep the system running stably and realize power-coordinated control when the working condition of these system changes.
2. The circuit decomposition model based on PS-PWM control effectively reduces the difficulty of analyzing TAB-DCER. In addition, the use of a genetic algorithm reduces the complexity and computational difficulty of the mathematical model for optimization of the RMS value of the inductor current.
3. The GAOS control strategy proposed in this paper can effectively reduce the sum of squares of the RMS value of the inductor current, decrease converter pass-state losses of the TAB-DCER, and improve the power transfer efficiency of TAB-DCER.

The control strategy proposed in this paper does not take into account the effects of voltage mismatch on RMS values of the inductor current of the TAB-DCER. Consequently, our next study will prioritize how to reduce the RMS value of the inductor current during voltage mismatch.

**Author Contributions:** X.M. and Q.D. conceptualized the idea of this research project; G.S. and C.Z. discussed the power flow analysis of TAB-DCER-based DC microgrids; the proposed algorithm and control were designed by X.W. and Z.L.; the simulation and experimental verification were designed by Q.D. and H.W.; the paper was written by X.M., X.W. and Z.L. All authors have read and agreed to the published version of the manuscript.

**Funding:** This research was funded by the Science and Technology Project of State Grid Corporation of China "Low Redundancy Grid Structure and Development Mode of New Electricity Distribution System", grant number 5108-202218280A-2-2-XG.

**Data Availability Statement:** The data used to support the research results of this paper are included within the article.

**Conflicts of Interest:** Author Xiaoli Meng, Qing Duan, Guanglin Sha, Caihong Zhao and Haoqing Wang was employed by the company China Electric Power Research Institute. The remaining authors declare that the research was conducted in the absence of any commercial or financial relationships that could be construed as a potential conflict of interest.

## References

1. Wu, H.F.; Zhang, J.J.; Xing, Y. A family of multiport buck-boost converters based on DC-link-Inductors (DLIs). *IEEE Trans. Power Electron.* **2015**, *30*, 735–746. [CrossRef]
2. Loh, P.C.; Li, D.; Chai, Y.K.; Blaabjerg, F. Autonomous operation of hybrid microgrid with AC and DC subgrids. *IEEE Trans. Power Electron.* **2013**, *28*, 2214–2223. [CrossRef]
3. Pham, V.-L.; Wada, K. Applications of Triple Active Bridge Converter for Future Grid and Integrated Energy Systems. *Energies* **2020**, *13*, 1577. [CrossRef]
4. Yu, Y.; Masumoto, K.; Wada, K.; Kado, Y. A DC Power Distribution System in a Data Center Using a Triple Active Bridge DC-DC Converter. *IEEJ J. Ind. Appl.* **2018**, *7*, 202–209. [CrossRef]
5. Yu, Y.; Masumoto, K.; Wada, K.; Kado, Y. Power Flow Control of a Triple Active Bridge DC-DC Converter Using GaN Power Devices for a Low-Voltage DC Power Distribution System. In Proceedings of the 2017 IEEE 3rd International Future Energy Electronics Conference and ECCE Asia (IFEEC 2017—ECCE Asia), Taiwan, China, 3–7 June 2017; pp. 772–777.
6. Smith, Z.T.; Beddingfield, R.B.; Grainger, B.M. Power Flow Control for Decoupled Load Performance of Current-Fed Triple Active Bridge Converter. *IEEE Open J. Power Electron.* **2023**, *4*, 319–329. [CrossRef]
7. Cai, Y.; Gu, C.; Li, J.; Yang, J.; Buticchi, G.; Zhang, H. Dynamic Performance Enhancement of a Triple Active Bridge with Power Decoupling-Based Configurable Model Predictive Control. *IEEE Trans. Transp. Electrif.* **2023**, *9*, 3338–3349. [CrossRef]
8. Kimura, Y.; Yanagi, Y.; Iwaya, K.; Miyazaki, T. A Method for Decoupling Current Control of Three-port Isolated Converter. In Proceedings of the IECON 2018—44th Annual Conference of the IEEE Industrial Electronics Society, Washington, DC, USA, 21–23 October 2018; pp. 895–900.
9. Wang, W.; Wang, P.B.; Ma, T.Y.; Liu, H.P.; Wu, H. A simple decoupling control method for isolated three-port bidirectional converter in low-voltage dc microgrids. In Proceedings of the 2015 IEEE Energy Conversion Congress and Exposition (ECCE), Montreal, QC, Canada, 20–24 September 2015; pp. 3192–3196.
10. You, J.; Vilathgamuwa, M.; Ghasemi, N.; Gong, B. Elimination of current oscillation in isolated three-port power converters using active damping method. *IET Power Electron.* **2019**, *12*, 2802–2809. [CrossRef]
11. Wang, Y.F.; Han, F.Q.; Yang, L.; Xu, R.; Liu, R.X. A Three-Port Bidirectional Multi-Element Resonant Converter with Decoupled Power Flow Management for Hybrid Energy Storage Systems. *IEEE Access* **2018**, *6*, 61331–61341. [CrossRef]
12. Jiang, L.; Costinett, D. A triple active bridge DC-DC converter capable of achieving full-range ZVS. In Proceedings of the 2016 IEEE Applied Power Electronics Conference and Exposition (APEC), Long Beach, CA, USA, 20–24 March 2016; pp. 872–879.
13. Guo, P.; Wang, Y.; Bi, K.; Gao, C.; Zhang, G. Model Predictive Control for the Three-Port Isolated Bidirectional DC/DC Converter with Soft Switching. In Proceedings of the 2023 International Conference on Power System Technology (PowerCon), Jinan, China, 21–22 September 2023; pp. 1–6.
14. Zhao, C.; Kolar, J.W. A novel three-phase three-port UPS employing a single high-frequency isolation transformer. In Proceedings of the 2004 IEEE 35th Annual Power Electronics Specialists Conference (IEEE Cat. No.04CH37551), Aachen, Germany, 20–25 June 2004; pp. 4135–4141.
15. Zhao, C.; Round, S.D.; Kolar, J.W. An isolated three-port bidirectional DC-DC converter with decoupled power flow management. *IEEE Trans. Power Electron.* **2008**, *23*, 2443–2453. [CrossRef]
16. Purgat, P.; Bandyopadhyay, S.; Qin, Z.; Bauer, P. Zero Voltage Switching Criteria of Triple Active Bridge Converter. *IEEE Trans. Power Electron.* **2021**, *36*, 5425–5439. [CrossRef]
17. Yu, X.P.; Lan, Z.; Zeng, J.H.; Tu, C.M.; He, D. Time-Domain-Based Superposition Analysis for Triple Active Bridge and Its Application for ZVS and Current Stress Optimization. *IEEE Trans. Power Electron.* **2023**, *38*, 5844–5857. [CrossRef]
18. Dey, S.; Mallik, A. Multivariable-Modulation-Based Conduction Loss Minimization in a Triple-Active-Bridge Converter. *IEEE Trans. Power Electron.* **2022**, *37*, 6599–6612. [CrossRef]

19. Zhou, L.; Gao, Y.; Ma, H.; Krein, P.T. Wide-Load Range Multiobjective Efficiency Optimization Produces Closed-Form Control Solutions for Dual Active Bridge Converter. *IEEE Trans. Power Electron.* **2021**, *36*, 8612–8616. [CrossRef]
20. Li, J.; Luo, Q.M.; Mou, D.; Wei, Y.Q.; Sun, P.J.; Du, X. A Hybrid Five-Variable Modulation Scheme for Dual-Active-Bridge Converter with Minimal RMS Current. *IEEE Trans. Ind. Electron.* **2022**, *69*, 336–346. [CrossRef]
21. Hebala, O.M.; Aboushady, A.A.; Ahmed, K.H.; Abdelsalam, I. Generic Closed-Loop Controller for Power Regulation in Dual Active Bridge DC–DC Converter with Current Stress Minimization. *IEEE Trans. Ind. Electron.* **2019**, *66*, 4468–4478. [CrossRef]
22. Li, J.; Luo, Q.M.; Luo, T.; Mou, D.; Liserre, M. Efficiency Optimization Scheme for Isolated Triple Active Bridge DC–DC Converter with Full Soft-Switching and Minimized RMS Current. *IEEE Trans. Power Electron.* **2022**, *37*, 9114–9128. [CrossRef]
23. Ibrahim, A.A.; Zilio, A.; Younis, T.; Biadene, D.; Caldognetto, T.; Mattavelli, P. Artificial Neural Networks Approach for Reduced RMS Currents in Triple Active Bridge Converters. In Proceedings of the IECON 2022—48th Annual Conference of the IEEE Industrial Electronics Society, Brussels, Belgium, 17–20 October 2022; pp. 1–6.
24. Ibrahim, A.A.; Zilio, A.; Biadene, D.; Caldognetto, T.; Mattavelli, P. Optimization Approaches for RMS Current Reduction of Triple Active Bridge Converters. In Proceedings of the 2023 IEEE Conference on Power Electronics and Renewable Energy (CPERE), Luxor, Egypt, 19–21 February 2023; pp. 1–7.